THE JOURNAL OF PHYSICAL CHEMISTRY C
A JOURNAL OF THE AMERICAN CHEMICAL SOCIETY

pubs.acs.org/JPCC

Article

Electrooxidation of CO on Platinum Nanoparticles Supported on NiO Thin Films

Aigerim Galyamova ⊥ Hyunwoo Ha ⊥ Graeme Henkelman and Richard M. Crooks

Cite This: J Phys Chem C 2023 127 7107−7118

Read Online

ABSTRACT: In this article, we report on a robust experimental model to investigate strong metal−support interactions (SMSI) and their effect on electrocatalytic reactions in the absence and presence of direct contact between the nanoparticles (NPs) and the metal oxide thin film. Specifically, we describe beneficial interactions between $Ni_{0.9}O$ thin film supports and PtNPs toward the CO electrooxidation reaction. The metal oxide layer ($Ni_{0.9}O$) is prepared by atomic layer deposition and characterized using X-ray photoelectron spectroscopy (XPS). PtNPs, containing an average of either 55 (Pt_{55}) or 140 (Pt_{140}) atoms, were synthesized using a dendrimer encapsulation method. The results indicate negative shifts of ∼100 and ∼60 mV of the CO electrooxidation peak potential when $Ni_{0.9}O$ thin films are in contact with Pt_{55} NPs and Pt_{140} NPs, respectively. Additionally, the oxygen evolution reaction (OER) is suppressed only when the PtNPs are in contact with the $Ni_{0.9}O$ thin film. Density functional theory (DFT) calculations indicate that both the CO electrooxidation enhancement and suppression of the OER can be attributed to a 1.23 eV decrease of the CO binding energy and a 0.35 eV increase of the OH binding energy at a NiO(111)/Pt_{55} NP interface compared to isolated Pt_{55} NPs.

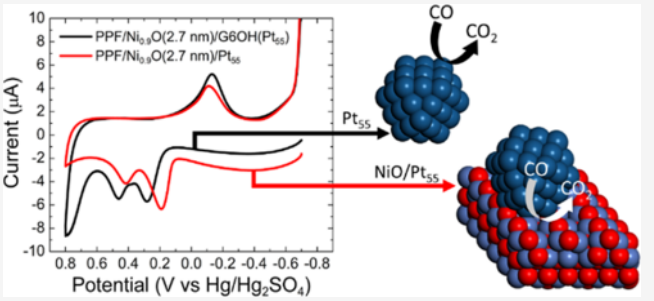

INTRODUCTION

Here, we report on significantly improved electrocatalytic activity for the carbon monoxide (CO) electrooxidation reaction on Pt nanoparticles (NPs) supported on $Ni_{0.9}O$ thin films compared to the same electrode in the absence of support interactions. This work builds upon earlier studies from our groups in which we demonstrated that density functional theory (DFT) was effective for predicting the nature of metal/support interactions for the electrochemical oxygen reduction reaction (ORR). Specifically, we found increased ORR activity and a change in the number of effective electrons transferred for two different metal oxide/NP combinations: SnO_x/AuNPs and TiO_y/AuNPs.[1,2] The present study indicates that the theoretical/experimental approach used for electrochemical reductions is also applicable to electrooxidation reactions. Electrooxidation reactions are of high interest for applications in direct methanol fuel cells, where the efficiency and stability of the fuel cell are limited by carbon monoxide poisoning.[3] Furthermore, DFT analysis of CO oxidation requires two descriptors, rather than the single descriptor used for the ORR, thereby expanding the complexity of the theory required for comparison to experiments.[4]

As alluded to above, we have previously reported on an experimental model that enables investigation of the effects of strong metal−support interactions (SMSI) on the electrocatalytic performance of metal NPs in the absence and presence of direct contact with metal oxide thin films.[1,2,5−8] This model is illustrated in Scheme 1, where two distinct electrocatalytic configurations are shown.

In Scheme 1(left), the principal electrocatalyst is a dendrimer-encapsulated NP (DEN).[9−11] Here, the dendrimer prevents direct contact between the metal NP and the underlying metal oxide thin film resulting in an electrocatalytic response that arises exclusively from the metal NP. The configuration in Scheme 1 (right) shows that after removal of the dendrimer, direct contact between the NP and the metal oxide thin film is established. Depending on the nature of the metal oxide, changes in the electrocatalytic properties of the NP might be observed.

In the past, we have shown that TiO_y (y = 1.9; 2.0) thin-film-supported AuNPs (Scheme 1, right) exhibit enhanced ORR activity compared to AuNPs in the absence of support interactions (Scheme 1, left).[2] DFT predicted a priori that this enhancement would occur due to partial charge transfer from oxygen vacancies in the TiO_y to AuNPs, where the corner edge of the supported Au_{147} NP was the active site for ORR. Indeed, we confirmed the existence of such charge transfer

Received: November 24, 2022
Revised: March 8, 2023
Published: April 11, 2023

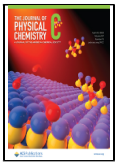

https://doi.org/10.1021/acs.jpcc.2c08254
J Phys Chem C 2023 127 7107−7118

Scheme 1. Illustration of the Experimental Model

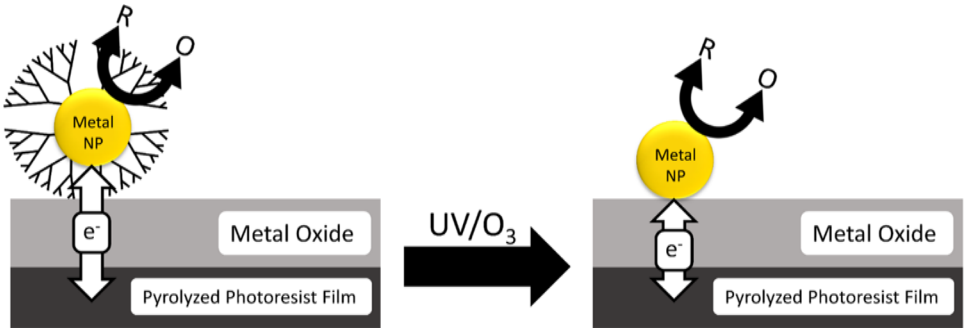

experimentally using X-ray photoelectron spectroscopy (XPS). In contrast to TiO_y, a nonreducible oxide thin film like Al_2O_3 does not alter the electrocatalytic performance of PtNPs for either the ORR or CO electrooxidation.[6,7]

In the present study, we continue our systematic examination of the effect of SMSI on electrocatalysis by focusing on the electrooxidation of CO. In this case, DFT calculations indicated favorable interactions on NiO-supported PtNPs. NiO-supported Pt materials have previously been investigated for gas-phase CO oxidation. For example, Somorjai and co-workers studied the rates of gas-phase CO oxidation at PtNPs supported on mesoporous oxides.[12] They found the highest CO oxidation enhancement rates on Co_2O_3 and NiO. The observed enhancement was attributed to the Mars−van Krevelen (MvK) mechanism,[13] wherein the lattice oxygen of the supporting oxide directly participates in the oxidation of CO. This mechanism is often associated with oxidation or electrooxidation reactions that take place on oxygen vacancy-containing metal oxide supports.[13]

Electrocatalytic reactions, including electrooxidation of formic acid and alcohols, have also been studied using NiO-supported Pt materials. For example, Duarte and co-workers investigated ethanol electrooxidation using a physical mixture of Pt and NiO NPs.[14] The results indicated an increase in the current density, as well as a small negative shift in the onset potential, for Pt and NiO NPs compared to Pt-only NPs. The enhancement was attributed to a bifunctional mechanism, wherein the proximity of Pt and NiO facilitated the removal of carbon monoxide, a byproduct of ethanol oxidation.

We investigated CO electrooxidation activity on $Ni_{0.9}O$ thin-film-supported PtNPs using the following experimental method. First, ∼2.7 nm of $Ni_{0.9}O$ was deposited over a pyrolyzed photoresist film (PPF)[15] electrode using atomic layer deposition (ALD). Second, Pt DENs[11,16,17] composed of an average of 55 (Pt_{55}) or 140 (Pt_{140}) atoms were immobilized onto this support. Third, the resulting construct (Scheme 1, left) and the configuration following dendrimer removal (Scheme 1, right) were evaluated for CO electrooxidation activity. The Pt_{55} electrocatalysts exhibited a favorable potential shift of ∼100 mV for CO electrooxidation when the NPs were directly in contact with the $Ni_{0.9}O$ thin film compared to when support interactions were absent. In the case of the larger Pt_{140} NPs, a negative shift of ∼60 mV was observed. Surface analysis by XPS revealed no change in the electronic state of the PtNPs regardless of whether they were in contact with the $Ni_{0.9}O$ thin film.

After obtaining the experimental results, we performed DFT calculations to estimate CO electrooxidation reaction pathways for isolated cuboctahedral (COh) Pt_{55} NPs, NiO(111) slab, and COh Pt_{55} NPs supported on NiO(111) slab (NiO(111)/Pt_{55}). Specifically, the direct, Eley−Rideal and Langmuir−Hinshelwood mechanisms for the CO electrooxidation reaction were considered. The binding energy of reactants and the formation energy of intermediates and products were calculated for each reaction mechanism. A Bader charge analysis[18] of the isolated Pt_{55} NP and NiO(111)/Pt_{55} constructs provided insight into the reactivity of the CO electrooxidation reaction at the active sites for each material. The DFT calculations indicate that the interfacial site of the NiO(111)/Pt_{55} system has optimal binding energies for the adsorbed reactants (CO and OH) that decrease the CO electrooxidation overpotential by ∼350 mV compared to unsupported Pt_{55} NP.

METHODS

Chemical and Materials. The following chemicals were used as received: $HClO_4$ (70+ , ultrapure grade, J. T. Baker, Phillipsburg, NJ); NaOH (1.0 M, Fischer Scientific, Waltham, MA); $CuSO_4$ (98 , anhydrous, Acros Organics, Morris Plains, NJ); $NaBH_4$ (99.99 trace metals basis, MilliporeSigma, Saint Louis, MO); K_2PtCl_4 (99.99 trace-metal basis, Acros Organics); bis(*N*,*N*′-di-*t*-butylacetamidinato)nickel(II) (NiAMD, 99.999 , STREM Chemicals, Inc., Newburyport, MA). The following compressed gases were purchased from Linde (Austin, TX): high-purity Ar (99.998), high-purity CO (99.5), and forming gas (5 H_2/95 N_2).

Sixth-generation hydroxy-terminated (G6OH) poly(amidoamine) dendrimers were purchased as 12.98 wt methanol solution from Dendritech, Inc. (Midland, MI). For the DEN synthesis, 100.0 μM aqueous dendrimer solution was prepared by removing methanol from the stock solution under vacuum and reconstituting the dendrimers in water. Ultrahigh-performance liquid chromatography (UHPLC)-grade water (MilliporeSigma) was used for dendrimer reconstitution, DEN syntheses, and aqueous solutions preparation.

For PPF fabrication, fused quartz slides (GE 124, 3″ mm × 1″ mm × 1 mm) were purchased from Technical Glass Products, Inc. (Painesville Twp, OH). Photoresist (AZ 1518) and photoresist developer (AZ 400K, 1:4) were purchased from Integrated Micro Materials (Argyle, TX).

Fabrication of Pyrolyzed Photoresist Film PPF) Electrodes. PPF electrodes were fabricated following a previously reported procedure that can be found elsewhere.[2]

Deposition of Nickel Oxide Thin Films on PPF Electrodes. The nickel oxide thin films were deposited as follows using a Savannah S100 Cambridge NanoTech ALD system (Ultratech, San Jose, CA). First, the nickel precursor, NiAMD, was heated to 125 °C. Second, PPF electrodes were

https://doi.org/10.1021/acs.jpcc.2c08254
J Phys Chem C 2023 127 7107−7118

placed in the ALD chamber and heated to 150 °C for 600 s under a constant N_2 flow (20 sccm). Third, the heated PPF electrodes were exposed to ten 0.015 s pulses of O_3; each O_3 pulse was followed with a 20 s N_2 purge. This treatment introduces oxygen functionalities onto the PPF surfaces, hence facilitating the metal oxide deposition.[1] Fourth, an ALD cycle was carried as follows: (1) 0.015 s pulse of O_3; (2) 30.0 s purge with N_2; (3) 0.75 s pulse of NiAMD; and (4) 30.0 s purge with N_2. These four steps were repeated until the desired number of cycles or film thickness were obtained. We determined that this procedure results in the formation of nickel oxide thin films having a Ni/O ratio of 0.9:1.0 ($Ni_{0.9}O$) using XPS.

Synthesis and Immobilization of Pt DENs. Two different Pt DEN sizes, G6OH(Pt_{55}) and G6OH(Pt_{140}), were synthesized using a previously described galvanic exchange method.[6,11,19,20] The number of Pt atoms was chosen to follow magic number formulas for the COh shape.[21] The two Pt DEN syntheses were normalized to have equal Pt loadings. That is, both G6OH(Pt_{55}) and G6OH(Pt_{140}) DEN solutions contained the same atomic concentration of Pt. 10.0 μM G6OH(Pt_{55}) DEN solutions were prepared using a slightly modified version of the procedure described in our previous publications.[5,8] A brief summary of this process can be found in the Supporting Information (SI). This synthesis produced zero-valent PtNPs (Figure S1a in the SI) with an average size of 1.3 ± 0.2 nm (Figure S2a,b in the SI). 3.92 μM G6OH(Pt_{140}) DEN solutions were synthesized using a previously reported multistep galvanic exchange method.[19] The full description of this process can be found in the SI. This synthesis produced zero-valent PtNPs (Figure S1b in the SI) having an average size of 1.8 ± 0.3 nm (Figure S2c,d in the SI). The experimentally observed Pt_{55} and Pt_{140} NP diameters closely match the reported sizes for COh-shaped PtNPs containing the same number of atoms, respectively.[22]

The G6OH(Pt_{55}) or G6OH(Pt_{140}) DENs were immobilized onto the PPF and PPF/$Ni_{0.9}O$ surfaces by immersion of the supports into the DEN solution for 45 min. Following immobilization, the resulting modified supports (PPF/G6OH-(Pt_{55}), PPF/G6OH(Pt_{140}), PPF/$Ni_{0.9}O$/G6OH(Pt_{55}), or PPF/$Ni_{0.9}O$/G6OH(Pt_{140})) were rinsed with UHPLC water, dried under an Ar flow, and left to equilibrate under ambient lab atmosphere for at least 1 h prior to use. Our previous results indicated that this immobilization procedure results in ~15 of the electrode surfaces being covered with Pt DENs.[5,23]

UV/O_3 Method for Decomposition of G6OH Dendrimers. Dendrimers were removed from the surfaces of the modified supports following a previously reported UV/O_3 dendrimer decomposition procedure.[6] The resulting PPF/Pt_{55}-, PPF/Pt_{140}-, PPF/$Ni_{0.9}O$/Pt_{55}-, and PPF/$Ni_{0.9}O$/Pt_{140}-modified supports were allowed to equilibrate under ambient lab atmosphere for at least 1 h before use.

Structural Characterization. A Kratos Axis Ultra DLD spectrometer (Chestnut Ridge, NY) was used for all XPS measurements. The XPS analyses were performed in the same manner as in our previous reports.[1,2] That is, the measurements were carried out ex situ for consistency and ease of comparison between studies. Briefly, the spectra were collected using an Al K source, 0.10 eV step size, and 20 eV band pass energy. CasaXPS (version 2.3.25PR1.0, Casa Software, Teignmouth, U.K.) was used for peak fitting and quantitative data analysis. Binding energies (BEs) were calibrated against the C 1s line of PPF (284.50 eV).[24] Symmetric line shapes were fitted using a mixed Gaussian/Lorentzian (GL(30)) model, while asymmetric line shapes were fitted using an asymmetric Lorentzian (LA(1.2,85,70)) model.

A J. A. Woollam M-2000D spectroscopic ellipsometer (Lincoln, NE) was used to determine the thicknesses of the $Ni_{0.9}O$ films. Data were collected between 45 and 65° with 5° increments and a 10 s dwell time at each step. A two-layer model was used for data analysis: the first layer was 500 nm of PPF and the second layer was $Ni_{0.9}O$ film. The $Ni_{0.9}O$ film thicknesses were allowed to vary. The optical constants for the materials were determined experimentally.

A JEOL-2010F transmission electron microscope (TEM) having a point-to-point resolution of 0.2 nm was used to collect TEM images. The TEM samples were prepared by pipetting 2.0 μL of the DEN solution onto a carbon-mesh-over-Cu TEM grid (Electron Microscopy Sciences, Hatfield, PA). Prior to the analysis, the TEM samples were dried overnight in the laboratory ambient atmosphere.

A Wyko NT9100 optical profilometer having a 0.1 nm vertical resolution was used to obtain topographic images of the PPF/$Ni_{0.9}O$ surfaces. The data were collected using 25.0× magnification over an area of 175 μm × 234 μm.

Electrochemical Characterization. All electrochemical measurements were performed in a custom-built Teflon electrochemical cell using a CHI 700E bipotentiostat, a glassy carbon rod counter electrode, and a Hg/Hg_2SO_4 reference electrode (Instruments, Inc., Austin, TX). The geometric area of the working electrode was constrained to 12.4 mm^2.[5]

Prior to the electrooxidative CO stripping experiments, all modified supports were electrochemically cleaned in an Ar-saturated, 0.10 M $HClO_4$ solution. Specifically, the electrode potential was scanned 10 times between −0.65 and 0.63 V at 0.050 V/s.

Following electrochemical cleaning, electrooxidative CO stripping experiments were performed as follows in a 0.10 M $HClO_4$ solution. First, a working electrode was held at −0.70 V for 2 min in CO-saturated, 0.10 M $HClO_4$ solution. Second, while continuing to hold the applied potential at −0.70 V, the working solution was purged with N_2 for 25 min, thereby displacing CO from the solution. Third, the electrode potential was scanned two times between −0.70 and 0.80 V at 0.050 V/s.

DFT Calculations. Generalized gradient approximation spin-polarized DFT calculations were carried out with the Vienna Ab initio Simulation Package (VASP) code[25] using the Perdew−Burke−Ernzerhof (PBE)[26] functional. The valence electron wave functions were expanded in a plane-wave basis up to a cutoff energy of 550 eV. The interaction between ionic core electrons and valence electrons was described by the projector augmented-wave (PAW) method.[27] The DFT + U formalism[28] with U_{eff} = 6.45 eV[29,30] was applied to Ni to treat the localized Ni 3d orbitals. The convergence criteria for the electronic structure and atomic geometry were set to 10^{-3} eV and 0.05 eV $Å^{-1}$, respectively. A Gaussian smearing function with a finite temperature width of 0.05 eV was used. The Γ point was used to sample the Brillouin zone.

The computationally optimized lattice constant of a_0 = 4.16 Å and magnetic moment on the Ni ions of M = 1.84 μ_B were calculated for the antiferromagnetic phase of bulk NiO.[30] The calculated values closely matched the experimental values of a_0 = 4.177 Å[31] and magnetic moment on the Ni ions of M = 1.77 − 2.26 μ_B.[32,33] Figure S3 in the SI shows the specific model structures used in our calculations. The NiO(111) surface was

https://doi.org/10.1021/acs.jpcc.2c08254
J Phys Chem C 2023 127 7107−7118

modeled with a four-layer slab with an oxygen-terminated 6 × 6 surface supercell. The bottom two NiO layers were frozen in their bulk position for the geometry optimization, and a 25 Å vacuum gap along the *z*-direction was applied to avoid interactions between the periodic slabs. The unsupported Pt_{55} NP was modeled with icosahedral (Ih) and COh structures. These two Pt_{55} NPs were modeled with all atoms relaxed and a 10 Å vacuum gap in all directions. The structure of the Pt_{55} NP supported on NiO(111) was determined via their stability. Specifically, the binding energy of the COh Pt_{55} NP (ΔE_{bind} = −19.18 eV) was found to be more stable than the Ih Pt_{55} NP (ΔE_{bind} = −15.08 eV) on the NiO(111) surface. Hence, we use COh Pt_{55} NP in our DFT calculations.

To calculate the CO electrooxidation activity, we considered the following six associative reaction steps

$$\Delta \ _1\text{: CO g) + H}_2\text{O l) } \leftrightarrow \text{ COOH + H}^+ + \text{e}^-)$$

$$\Delta \ _2\text{: COOH } \leftrightarrow \text{ CO}_2\text{ g) + H}^+ + \text{e}^-)$$

$$\Delta \ _3\text{: CO g) + H}_2\text{O l) } \leftrightarrow \text{ CO + H}_2\text{O l)}$$

$$\Delta \ _4\text{: CO + H}_2\text{O l) } \leftrightarrow \text{ COOH + H}^+ + \text{e}^-)$$

$$\Delta \ _5\text{: CO + H}_2\text{O l) } \leftrightarrow \text{ CO + OH + H}^+ + \text{e}^-)$$

$$\Delta \ \text{: CO + OH } \leftrightarrow \text{ COOH}$$

Different combinations of these steps represent various CO electrooxidation reaction pathways on the Pt_{55} NP and NiO(111) surface. Here, we focused on the direct,[34] Eley–Rideal (E–R)[35] and Langmuir–Hinshelwood (L–H)[36−38] mechanisms for the CO electrooxidation reaction on the isolated Pt_{55} NP, NiO(111) slab, and NiO(111)/Pt_{55} catalysts. These three reaction mechanisms have sequential reaction pathways of ΔG_1 and ΔG_2; ΔG_3, ΔG_4, and ΔG_2; and ΔG_3, ΔG_5, ΔG_6, and ΔG_2, respectively. The CO electrooxidation overpotential was found from the reaction energy pathway, calculated using eq 1[39]

$$\Delta G\ U) = \Delta \quad \Delta \text{ZPE} - T\Delta S - neU \tag{1}$$

where ΔE is the reaction energy, ΔZPE is the zero-point energy correction, ΔS is the change in entropy, *ne* is the number of electrons, and *U* is the applied potential. The chemical potential of the solvated proton and electron pair ($H^+ + e^-$) at standard conditions (p_{H_2} = 1 bar, a_{H^+} = 1, *T* = 298.15 K) was calculated as 0.5 $\mu^0_{H_2(g)} - eU$ by assuming equilibrium at the standard hydrogen electrode.[2,40,41]

RESULTS AND DISCUSSION

Properties of $Ni_{0.9}O$ Thin Films. In our previous studies, we showed that well-defined thickness, uniformity, stoichiometry, and stability of metal oxide thin films are critical for the purposes of our electrocatalysis experiments.[1,2,5,8] In this section, we examine each of those factors in relation to nickel oxide thin films deposited on PPF electrodes.

$Ni_{0.9}O$ film thicknesses were determined using ellipsometry. Specifically, a calibration curve was obtained by plotting measured thicknesses as a function of the number of ALD cycles performed (Figure S4 in the SI). The plot reveals a linear growth rate of 0.028±0.003 nm/cycle with a nucleation delay of three ALD cycles.[42] For the experiments discussed hereafter, $Ni_{0.9}O$ thin films were prepared using 100 ALD cycles, which results in ∼2.7 nm thick films.

The topography of ∼2.7 nm thick $Ni_{0.9}O$ films was determined using optical profilometry. Figure S5 in the SI shows a representative topographic image over an area of 175 μm × 234 μm. The average rms roughness of three independently prepared ∼2.7 nm thick $Ni_{0.9}O$ films was 1.0 ± 0.1 nm. This value is in agreement with literature studies of NiO films prepared by ALD and spray pyrolysis,[43,44] as well as our reports for Al_2O_3, SnO_x, and TiO_y films having similar thicknesses.[1,2,5]

The stoichiometry of ∼2.7 nm thick $Ni_{0.9}O$ films was determined using XPS. Specifically, the concentration of nickel vacancies in the $Ni_{0.9}O$ films was calculated using the ratio of atomic concentrations of Ni 2p and O 1s signals (Table S1 in the SI). Here, the O 1s signal was deconvoluted to obtain the fraction of oxygen bound to Ni, while the Ni 2p signal was used without additional processing (Figure S6 in the SI). This quantitative analysis revealed a Ni/O ratio of 0.9:1.0, indicating the presence of Ni vacancies in the lattice structure of the oxide.[45,46]

Previously we showed that the UV/O_3 dendrimer removal treatment can alter the stoichiometry of SnO_x films.[1] Accordingly, we investigated whether this also occurs with $Ni_{0.9}O$ films. Figure S7 and Table S2 in the SI summarize XPS measurements obtained for PPF/$Ni_{0.9}O$(2.7 nm) supports after the UV/O_3 dendrimer removal procedure. In this case, no changes in the Ni/O ratio were observed after exposure to UV/O_3.

The stability of ∼2.7 nm thick $Ni_{0.9}O$ films was tested under the same experimental conditions used for the electrocatalytic measurements described later. Specifically, a single PPF/$Ni_{0.9}O$(2.7 nm) electrode was subjected to the following stepwise procedure: (1) exposure to the same UV/O_3 procedure used for dendrimer removal and (2) a series of the same CV scans used for the CO electrooxidation study. The latter included 10 electrochemical cleaning scans and two electrooxidative CO stripping scans in 0.10 M $HClO_4$ solution. The stability of the electrode was evaluated by comparing the XPS signal of the Ni 2p and Ni 3p regions after each step within the same area of the electrode. Figure S8 in the SI shows an overlay of three XPS spectra. The black trace is from an as-deposited PPF/$Ni_{0.9}O$(2.7 nm) electrode, the red trace is from the same electrode after exposure to UV/O_3 (Step 1), and the blue trace was obtained after electrochemical scanning (Step 2). The results exhibit a very slight variation in signal intensity at 855.8 and 67.15 eV compared to the original signal obtained immediately after $Ni_{0.9}O$ film deposition. This is consistent with a small amount of surface oxidation induced by the UV/O_3 treatment.[47] Importantly, we do not observe a significant change in the integrated area (Table S3 in the SI), BE positions, or peak shape in the XPS spectra. We conclude that the ∼2.7 nm thick $Ni_{0.9}O$ films are sufficiently stable under the experimental conditions used for electrocatalytic measurements.

Unfortunately, it was not possible to use X-ray diffraction for characterization, because this technique requires films thicker than ∼20 nm for accurate analysis.[2] However, the type of NiO films used in this study have previously been reported to be amorphous.[48]

In summary, we demonstrated that $Ni_{0.9}O$ thin films deposited onto PPF electrodes have well-defined and

https://doi.org/10.1021/acs.jpcc.2c08254
J Phys Chem C 2023 127 7107−7118

reproducible thicknesses, uniformity, stoichiometry, and stability under the relevant experimental conditions.

Decomposition of G6OH Dendrimers. As alluded in the Introduction Section, our approach consists of evaluating the electrocatalytic response of the NPs in the absence (Scheme 1, left) and presence (Scheme 1, right) of support interactions. Hence, a method for dendrimer removal is required. In previous studies, XPS demonstrated that the organic dendrimer framework can be largely removed from G6OH-(Pt_{55}) DENs immobilized on Al_2O_3 or TiO_y thin films when they are exposed to UV/O_3.[6,8] Accordingly, we applied the same methodology to Pt DENs immobilized on the $Ni_{0.9}O$ thin films.

Figure S9a in the SI shows an overlay of XPS spectra in the N 1s region of a PPF/$Ni_{0.9}O$(2.7 nm)/G6OH(Pt_{55})-modified support before and after UV/O_3-induced dendrimer removal. Figure S9b in the SI provides analogous data for a PPF/$Ni_{0.9}O$(2.7 nm)/G6OH(Pt_{140})-modified support. Following the UV/O_3 dendrimer decomposition procedure, an 80 ± 5 decrease in the dendrimeric N 1s signal is observed for both PtNPs sizes. This number was calculated from the percentage difference of the N 1s area before and after the UV/O_3 dendrimer removal procedure using CasaXPS software.[6] This value is in good agreement with our previous observations for G6OH dendrimer removal on other metal oxide supports.[6,8]

Electrooxidative CO Stripping on PPF-Supported PtNPs. Prior to investigating PtNPs supported on $Ni_{0.9}O$ thin films, we validated the general experimental approach by studying CO electrooxidation at PtNPs supported on PPF, a carbon surface that is known to be inert for this reaction.[6] Figure 1a shows CVs for electrooxidative CO stripping on Pt_{55} NPs in the absence and presence of direct interactions with PPF electrode, that is, with and without the dendrimer present, respectively.

The CO electrooxidation peak (p1) during the forward scan of the PPF/G6OH(Pt_{55}) electrode is present at 0.19 ± 0.02 V. CO oxidation is followed by Pt oxide formation (p2 at 0.40 ± 0.03 V) and the onset of the oxygen evolution reaction (OER) at 0.80 V (p3).[49] Upon scan reversal, the Pt oxide reduction peak (p4) is present at −0.15 ± 0.02 V, and it is followed by H adsorption and the onset of the hydrogen evolution reaction (HER) at −0.60 V.[50] The observed CO electrooxidation peak position and other CV features are consistent with literature values for PtNP electrocatalysts.[51,52] Upon cycling the electrode potential a second time (Figure S10a in the SI), the CO electrooxidation peak at ∼0.19 V is absent. This confirms complete oxidation of CO during the first cycle. The H underpotential deposition adsorption/desorption features are poorly defined in the CVs because the PtNPs used in this study are so small. Similar results have been reported previously.[11,20,53]

Following the electrocatalytic measurements, the PPF/G6OH(Pt_{55}) electrode was subjected to the UV/O_3 dendrimer removal procedure, and the resulting PPF/Pt_{55}-modified electrocatalyst was tested for its CO electrooxidation activity. The corresponding CV in Figure 1a exhibits the same features as discussed earlier for the PPF/G6OH(Pt_{55}) electrode. For example, the CO electrooxidation peak occurs at the same position, 0.19 ± 0.02 V, as that of the PPF/G6OH(Pt_{55}) electrocatalyst. This indicates that UV/O_3 dendrimer removal procedure alone does not induce changes in the activity of Pt_{55} NPs for electrooxidative CO stripping. Note that the peak heights (p4) associated with CO electrooxidation are very nearly the same in Figure 1a. The slight decrease after dendrimer removal might be a consequence of a small amount of PtNP loss from the electrode surface due to the UV/O_3 dendrimer removal procedure.

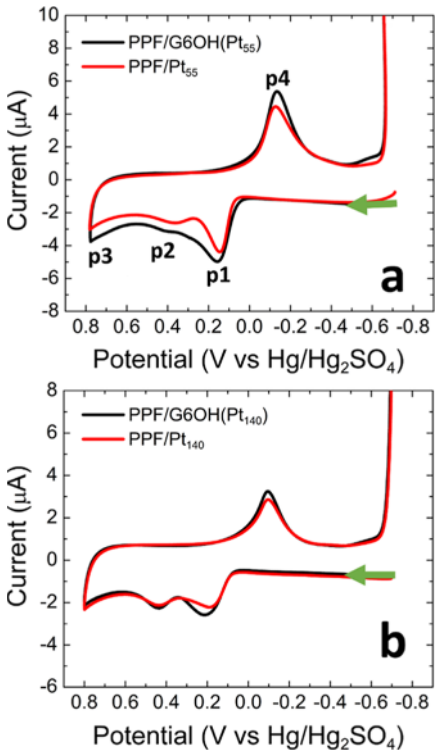

Figure 1. CVs obtained for electrooxidative CO stripping on (a) PPF/G6OH(Pt_{55}) and (b) PPF/G6OH(Pt_{140}) electrodes with and without the dendrimer present. The electrode potential was scanned between −0.70 and 0.80 V at 0.050 V/s. The solutions contained aqueous, 0.10 M $HClO_4$. The CVs were background-corrected using the linear transformation function of the Origin8 software to account for the differences in the capacitive currents between CVs. The experiments were carried out in triplicate for each electrode configuration using independently prepared electrodes to ensure reproducibility.

Figure 1b shows CVs for electrooxidative CO stripping on Pt_{140} NPs in the absence and presence of direct contact with the PPF electrode. The results are very similar to those observed for PPF/G6OH(Pt_{55}). In the forward scan direction, the CO electrooxidation peak occurs at 0.18 ± 0.01 V (p1). This is followed by the Pt oxide formation peak at 0.44 ± 0.02 V (p2), and the onset of the OER at 0.80 V (p3). During the reverse scan, the Pt oxide reduction peak occurs at −0.10 ± 0.01 V (p4), followed by H adsorption and the onset of the HER at −0.60 V. The second CV cycle for this electrode is shown in Figure S10b in the SI; the CO electrooxidation peak at ∼0.18 V is absent in this case also.

A comparison of the PPF/G6OH(Pt_{55}) and PPF/G6OH-(Pt_{140}) CVs in Figure 1 reveals the following. First, the CO electrooxidation peak occurs at slightly more negative potentials on Pt_{140} NPs. This is consistent with lower CO binding energies on larger PtNPs.[53,54] Second, the Pt oxide peak is ∼40 mV more positive for the Pt_{140} NPs. Likewise, the Pt oxide reduction peak is ∼50 mV less negative potentials for the Pt_{140} NPs. Both of these observations are consistent with lower binding energies of oxygen-containing species on larger PtNPs.[54,55]

https://doi.org/10.1021/acs.jpcc.2c08254
J Phys Chem C 2023 127 7107−7118

Following the electrocatalytic measurements, the dendrimer was removed from the PPF/G6OH(Pt_{140}) electrode, and the resulting PPF/Pt_{140}-modified electrocatalyst was tested for its CO electrooxidation activity. The corresponding CV in Figure 1b possesses features similar to those discussed for PPF/G6OH(Pt_{140}), where no changes in CO electrooxidation peak position are apparent after dendrimer removal.

The key points of the foregoing discussion are twofold. First, the features observed for the electrooxidative CO stripping CVs on Pt_{55}, and Pt_{140} NPs are consistent with literature reports for PtNPs electrocatalysts. Second, no significant changes are observed for the electrooxidative CO stripping peak positions on PtNPs in the absence and presence of direct contact with PPF electrodes for both NPs sizes. This suggests that to a first approximation, the PtNPs are unchanged before and after dendrimer removal.

In addition to the CO electrooxidation experiments, we have examined the electronic state of PtNPs supported on PPF electrodes before and after the UV/O_3 dendrimer removal procedure. The results of these experiments are summarized in Figure S1 in the SI. Briefly, Pt_{55} or Pt_{140} NPs supported on PPF, which is an inert surface, appear metallic before and after the UV/O_3 dendrimer removal procedure. These control experiments also demonstrate that the oxidation state of PtNPs is not affected by transfer to the XPS.

Electrooxidative CO Stripping on $Ni_{0.9}O$-Supported PtNPs. We now focus on electrocatalytic measurements obtained at PtNPs supported on $Ni_{0.9}O$ thin films. Figure 2a shows CVs for electrooxidative CO stripping on Pt_{55} NPs in the absence and presence of interactions with the ~2.7 nm thick $Ni_{0.9}O$ support.

A CV corresponding to the PPF/$Ni_{0.9}O$(2.7 nm)/G6OH-(Pt_{55})-modified electrocatalyst closely resembles the CV features discussed for PPF/G6OH(Pt_{55}) in Figure 1a. There are, however, three changes to the CV when the Pt_{55} NPs are brought into contact with the $Ni_{0.9}O$ support following dendrimer removal. First, the CO oxidation peak (p1) shifts negative by 100 ± 20 mV when Pt_{55} NPs are in direct contact with $Ni_{0.9}O$. This observation suggests a favorable interaction between Pt_{55} NPs and the underlying $Ni_{0.9}O$ support for the CO electrooxidation reaction.

Second, the Pt oxide peak (p2) shifts negative by 40 ± 20 mV when the Pt_{55} NPs are directly supported on the $Ni_{0.9}O$ thin film. In contrast to this shift, the position of the Pt oxide reduction peak (p4 at −0.13 ± 0.01 V) does not change in the absence and presence of contact between the Pt_{55} NPs and the $Ni_{0.9}O$ thin film. The latter observation suggests that the shift observed in the Pt oxide formation peak (p2) position is related to interactions between Pt_{55} NPs and the $Ni_{0.9}O$ support. This interaction changes the OH binding energy on the Pt surface (as discussed later in the DFT section). Specifically, the stronger OH binding energy on the Pt surface favors the formation of Pt oxides, thereby shifting the position of p2 in the negative direction. The absence of a corresponding shift in p4 is a consequence of the hysteresis between Pt oxide formation and corresponding reduction reactions.[56]

Third, the current originating from the OER (p3) decreases by 70 ± 5 when Pt_{55} NPs are directly supported on the $Ni_{0.9}O$ thin film compared to the case when support interactions are absent. This observation suggests that the interaction between Pt_{55} NPs and the underlying $Ni_{0.9}O$ support leads to suppression of the OER. The second CV cycle for the PPF/$Ni_{0.9}O$(2.7 nm)/G6OH(Pt_{55}) and the PPF/$Ni_{0.9}O$(2.7 nm)/Pt_{55}-modified electrodes are shown in Figure S11a,b in the SI, respectively. In both cases, the CO electrooxidation peak is absent during the second cycle.

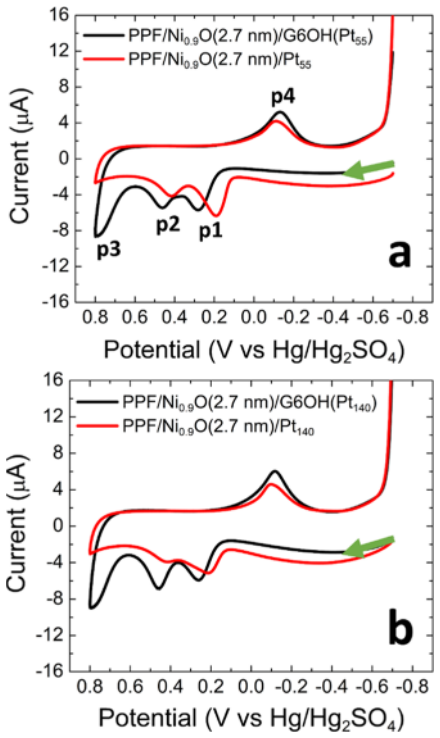

Figure 2. CVs obtained for electrooxidative CO stripping on (a) PPF/$Ni_{0.9}O$(2.7 nm)/G6OH(Pt_{55}) and (b) PPF/$Ni_{0.9}O$(2.7 nm)/G6OH(Pt_{140}) electrodes with and without the dendrimer present. The electrode potential was scanned between −0.70 and 0.80 V at 0.050 V/s. The solutions contained aqueous, 0.10 M $HClO_4$. The CVs were background-corrected using the linear transformation function of the Origin8 software. The experiments were carried out in triplicate for each electrode configuration using independently prepared electrodes to ensure reproducibility.

Figure 2b provides data analogous to that in Figure 2a, but for Pt_{140} NPs in the absence and presence of contact with the ~2.7 nm thick $Ni_{0.9}O$ film. In this case, the negative shift in the CO oxidation peak position is smaller, 60 ± 20 mV, but it is still unambiguously within the indicated uncertainty. As for the results in Figure 2a, the Pt oxide peak shifts 40 ± 20 mV in the negative direction, while the Pt oxide reduction peak (p4 at −0.11 ± 0.01 V) occurs at the same position regardless of the absence and presence of $Ni_{0.9}O/Pt_{140}$ interface. Likewise, the current originating from the OER (p3) decreases, in this case by 66 ± 8 . The second CV cycle for PPF/$Ni_{0.9}O$(2.7 nm)/G6OH(Pt_{140})- and PPF/$Ni_{0.9}O$(2.7 nm)/Pt_{140}-modified electrodes is shown in Figure S11c,d in the SI, respectively, in both cases, the CO electrooxidation peak is absent.

We carried out one additional experiment to ensure that no CO electrooxidation activity arises from the PPF/$Ni_{0.9}O$(2.7 nm) electrode when the PtNPs are absent. The results are shown in Figure S12 in the SI, and they confirm that the $Ni_{0.9}O$ surface is not catalytic for CO electrooxidation. This observation is consistent with theoretical calculations that are discussed in more detail later, but the key point is that they indicate strong binding of the reactants and intermediates to the NiO(111) surface (in the absence of PtNPs), thereby preventing electrooxidation of CO.

https://doi.org/10.1021/acs.jpcc.2c08254
J Phys Chem C 2023 127 7107−7118

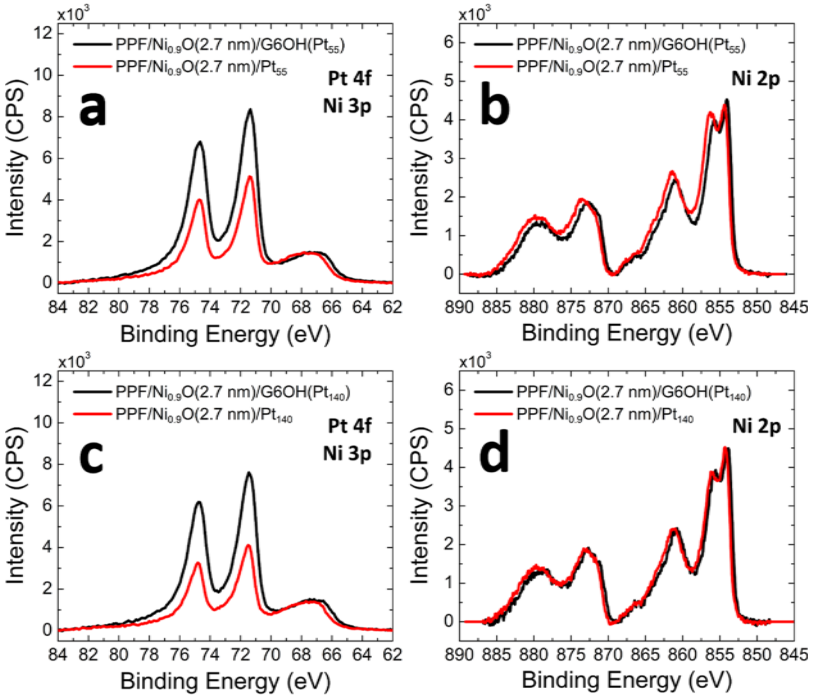

Figure 3. High-resolution XPS spectra in the Pt 4f, Ni 3p, and Ni 2p regions for the indicated electrode configurations. The XPS measurements were collected from the corresponding electrodes shown in Figure 2 following the CO electrooxidation experiments. XPS peaks were referenced to the position of the PPF C 1s peak at 284.50 eV.[24] The analysis was performed using three independently prepared electrodes.

The key conclusion of the foregoing discussion is that there are negative shifts of ∼100 and ∼60 mV in CO oxidation peak position and a significant decrease in OER activity when $Ni_{0.9}O$ thin film is directly in contact with Pt_{55} and Pt_{140} NPs, respectively.

Electronic Interactions between $Ni_{0.9}O$ Supports and PtNPs. XPS was used to determine the BEs of Pt 4f, Ni 3p, and Ni 2p before and after the UV/O_3 dendrimer removal procedure for PtNPs supported on the ∼2.7 nm thick $Ni_{0.9}O$ film.

The black traces in Figure 3a,b show the Pt 4f, Ni 3p, and Ni 2p regions for the PPF/$Ni_{0.9}O$(2.7 nm)/G6OH(Pt_{55})-modified electrode before UV/O_3 treatment.

The two Pt peaks are present at 71.35 eV (Pt $4f_{7/2}$) and 74.65 eV (Pt $4f_{5/2}$), which correspond to zero-valent Pt.[6,24,57] The small, broad peak at 67.15 eV originates from the Ni 3p signal (Figure S8 in the SI).[24,58] In the Ni 2p region (Figure 3b), the spectrum is complex due to multiplet splitting and satellite peaks that are characteristic of NiO.[58] The main two Ni peaks are present at 854.05 eV (Ni $2p_{3/2}$) and 872.75 eV (Ni $2p_{1/2}$). These peak positions and their separation indicate the dominance of the Ni^{2+} oxidation state.[58]

Following the initial XPS analysis, the same PPF/$Ni_{0.9}O$(2.7 nm)/G6OH(Pt_{55})-modified electrode was subjected to the UV/O_3 dendrimer removal procedure to ensure direct contact between the Pt_{55} NPs and the $Ni_{0.9}O$ support. Note that any Pt oxide that might have resulted from the UV/O_3 treatment was reduced back to metallic Pt using electrochemical cleaning prior to XPS analysis (see the Methods section and Figure S13 in the SI).[6]

The red spectra in Figure 3a,b correspond to Pt 4f, Ni 3p, and Ni 2p regions for the PPF/$Ni_{0.9}O$(2.7 nm)/Pt_{55}-modified electrode after UV/O_3 treatment for dendrimer removal and electrochemical cleaning. Pt peaks occur at the same positions as they do in the dendrimer-encapsulated Pt_{55} NPs. In the case of Ni 3p and Ni 2p regions, there is a 0.37 eV shift toward higher BEs when the Pt_{55} NPs are directly supported on $Ni_{0.9}O$ thin film.

Figure 3c,d provides data analogous to that in Figure 3a,b, but for Pt_{140} NPs in the absence and presence of contact with the $Ni_{0.9}O$ film. The black traces for Pt 4f, Ni 3p, and Ni 2p appear identical in terms of peak positions and shapes as for PPF/$Ni_{0.9}O$(2.7 nm)/G6OH(Pt_{55})-modified electrode. The red traces reveal no change in Pt 4f peaks positions, but there is a 0.25 eV shift toward higher BEs for both the Ni 3p and Ni 2p peaks when the Pt_{140} NPs are in contact with $Ni_{0.9}O$ thin film compared to when support interactions are absent.

To summarize, no changes in the electronic state of the PtNPs are observed regardless of whether they are or are not in contact with the $Ni_{0.9}O$ supports. In contrast, the Ni 3p and Ni 2p peaks shift toward higher BEs by 0.37 and 0.25 eV when $Ni_{0.9}O$ thin film directly supports Pt_{55} NPs and Pt_{140} NPs, respectively. Importantly, the Ni 3p and Ni 2p peak positions do not change for PPF/$Ni_{0.9}O$ (2.7 nm) electrodes (no PtNPs) following the UV/O_3 dendrimer removal procedure (Figure S8 in the SI). Hence, the observed shifts in Ni 3p and Ni 2p for PPF/$Ni_{0.9}O$/Pt_{55}- and PPF/$Ni_{0.9}O$/Pt_{140}-modified supports are likely related to electronic equilibration between the PtNPs and $Ni_{0.9}O$ thin films.

DFT Calculation of CO Electrooxidation Activity on the NiO 111) Surface. We now turn our attention to the theoretical verification of the foregoing experimental results. First, we considered the activity of the NiO(111) surface toward the CO electrooxidation reaction. As Norskov has suggested, the binding energy of reaction intermediates, ΔG_{bind}, can be an appropriate descriptor of the electrochemical reaction activity.[59−62] Accordingly, Figure S14 in the SI shows Gibbs free energy diagrams for the direct, E−R, and L−H CO electrooxidation reaction pathways on the NiO(111) surface. We found that, on the NiO(111) surface, the strong binding

https://doi.org/10.1021/acs.jpcc.2c08254
J Phys Chem C 2023 127 7107−7118

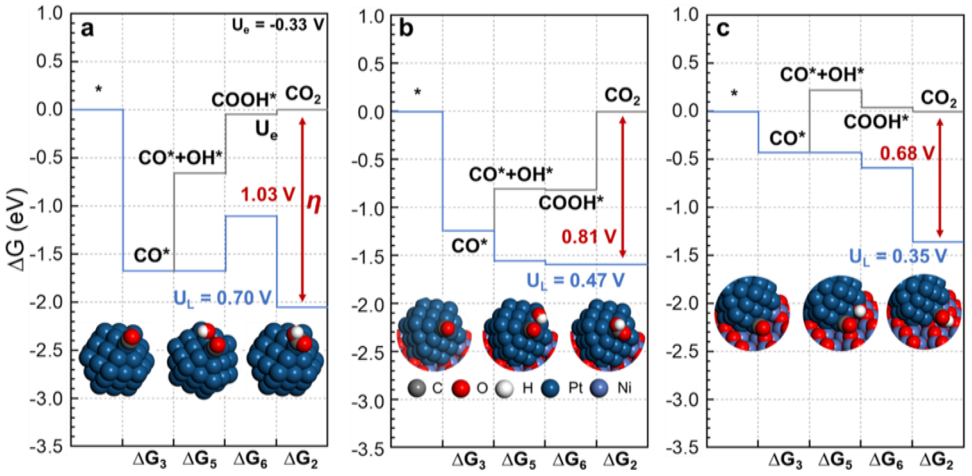

Figure 4. Gibbs free energy diagrams for the L–H CO electrooxidation reaction pathway on the surface of (a) an isolated Pt_{55} NP, (b) the top vertex site of the Pt_{55} NP supported on NiO(111), and (c) at the interfacial site between the Pt_{55} NP and NiO(111). Black and blue solid lines represent the DFT-estimated Gibbs free energy at the equilibrium potential (U_e) and limiting potential (U_L), respectively. The red solid line denotes the overpotential (η) for each system.

Table 1. DFT-Calculated Binding and Formation Energies and Electrochemical Potentials Corresponding to Figure 4

	surface on Pt_{55} NP	surface on NiO(111)/Pt_{55}	interface of NiO(111)/Pt_{55}
binding energy of CO (ΔG_{bind}, eV)	1.69	−1.24	−0.46
binding energy of OH (ΔG_{bind}, eV)	0.46	−0.10	0.11
formating energy of COOH (ΔG_6, eV)	0.57	−0.02	−0.16
limiting potential (U_L, V)	0.70	0.47	0.35
overpotential (η, V)	1.03	0.81	0.68

[a]The overpotential values are calculated from: overpotential (η) = −0.33 (U_e) − limiting potential (U_L).

energies of CO (ΔG_{bind} = −1.87 eV) and OH (ΔG_{bind} = −4.83 eV) lead to a high formation energy for COOH (ΔG_6 = 0.80 eV) and a high overpotential for CO_2 production (η = 5.35 V) at the equilibrium potential, U_e = −0.33 V (Table S4 in the SI). This means that on the NiO(111) surface, the reactants and intermediates have strong binding energies that prevent the release of the reaction product CO_2. Thus, NiO(111) surface is inert toward the CO electrooxidation reaction. This result is in agreement with previously discussed experimental observations (Figure S12 in the SI). Furthermore, the extremely strong binding energies of CO and OH on the NiO(111) surface limit the possibility of CO electrooxidation via a bifunctional mechanism in the NiO(111)/Pt_{55} system. That is, the reactants are too strongly bound to NiO(111) surface for them to migrate to an active site where CO electrooxidation can take place.[63]

DFT Calculation of CO Electrooxidation Activity on Pt_{55} NPs. Under the experimentally relevant conditions, the CO electrooxidation reaction on PtNPs is most likely to occur via the L–H mechanism, where COOH has been widely accepted in the literature as an intermediate molecule.[63−65] Hence, we use the L–H reaction pathway, ΔG_3, ΔG_5, ΔG_6, and ΔG_2, in the computational part of this study.

Figure 4a shows the Gibbs free energy diagram for the L–H reaction pathway at the active site of the isolated Pt_{55} NP. Table 1 summarizes the binding energies and the electrochemical potentials corresponding to Figure 4.

On the unsupported Pt_{55} NP, all reactants preferentially bind at the vertex and edge sites of the NP.[66] We found that on the Pt_{55} NP, the strong binding energy of CO (ΔG_{bind} = −1.69 eV) inhibits the formation of the COOH intermediate and hence the production of CO_2, making ΔG_2 a rate-limiting step for the CO electrooxidation reaction. This conclusion is in agreement with the literature reports.[65,67−69] Furthermore, the strong binding of CO weakens the binding of OH in ΔG_5 and causes an endothermic reaction of COOH formation in ΔG_6. In the case of the isolated Pt_{55} NP, the overpotential (η of the CO electrooxidation reaction is calculated to be 1.03 V.

In summary, we and others[59,63] have found that the binding energies of CO and OH control the CO electrooxidation activity on PtNPs. Therefore, tuning the binding energies of CO and OH can be the key to improving the activity of CO electrooxidation on PtNP electrocatalysts.

DFT Calculation of CO Electrooxidation Activity on NiO 111)/Pt_{55}. In this section, we examine the NiO(111)/Pt_{55} system and its activity for the CO electrooxidation reaction. Specifically, we considered two different active sites of the NiO(111)/Pt_{55} system: the top vertex site of the Pt_{55} NP supported on NiO(111), and the interfacial site between the Pt_{55} NP and NiO(111).

Figure 4b shows the Gibbs free energy diagram for the L–H CO electrooxidation reaction pathway on the top vertex site of the Pt_{55} NP supported on NiO(111). The comparison of the CO electrooxidation reaction pathway of the isolated Pt_{55} NP and the Pt_{55} NP supported on NiO(111) reveals the following. In both cases, the rate-limiting step is ΔG_2. However, the binding energy of CO at the vertex site on the Pt_{55} NP supported on NiO(111) (ΔG_{bind} = −1.24 eV) is weaker than the binding energy of CO on the unsupported Pt_{55} NP surface (ΔG_{bind} = −1.69 eV). In contrast, a stronger binding energy of OH is calculated at the vertex site on the Pt_{55} NP supported on NiO(111) (ΔG_{bind} = −0.10 eV) compared to the

https://doi.org/10.1021/acs.jpcc.2c08254
J Phys Chem C 2023 127 7107−7118

binding energy of OH on the isolated Pt_{55} NP (ΔG_{bind} = 0.46 eV). The weaker binding of CO and the stronger binding of OH on the top vertex site of the Pt_{55} NP supported on NiO(111) favor the formation of COOH (ΔG_6 = −0.02 eV) leading to a more negative overpotential for the CO electrooxidation reaction (η = 0.81 V) compared to the isolated Pt_{55} NP (η = 1.03 V). This result indicates a favorable interaction between Pt_{55} NP and NiO(111) for the CO electrooxidation reaction compared to the isolated Pt_{55} NP. Moreover, as Ooka H. reported, considering that an ideal catalyst has a free energy of reaction intermediate (ΔG_{RI}) of zero (ΔG_{RI} = 0),[70] the relationship between the binding energy and overpotential of the intermediate product in our result can also be interpreted based on the correlation of ΔG_{RI} and overpotential. Accordingly, ΔG_{RI} remains a useful descriptor for predicting catalytic activity.[39,70−72]

Figure 4c provides data analogous to that in Figure 4b, but for the interfacial site between Pt_{55} NP and NiO(111). In this case, the interfacial site of NiO(111)/Pt_{55} exhibits the weakest binding energy of CO (ΔG_{bind} = −0.46 eV) and intermediate binding energy of OH (ΔG_{bind} = 0.11 eV) compared to the top vertex site of the Pt_{55} NP supported on NiO(111) or the isolated Pt_{55} NP. Among the tested model structures, the interfacial site of NiO(111)/Pt_{55} has the most favorable formation energy for COOH (ΔG_6 = −0.16 eV), and a more negative overpotential for the CO electrooxidation reaction (η = 0.68 V). This indicates that the interfacial site of NiO(111)/Pt_{55} catalyst has the most appropriate binding energies for CO and OH to form products according to Sabatier's principle.[73,74]

In addition to the calculation discussed above, we estimated the CO electrooxidation activity of our model structures through the direct (Table S5 in the SI) and the E−R (Table S6 in the SI) mechanisms. In all cases, the interfacial site between Pt_{55} NP and NiO(111) has more negative overpotential values, and hence higher activity toward CO electrooxidation reaction, compared to the isolated Pt_{55} NP.

The key point of the foregoing discussion is that DFT analysis indicates enhanced CO electrooxidation activity of the Pt_{55} NP supported on NiO(111) slab compared to the isolated Pt_{55} NP. Specifically, theoretical calculations estimate a negative shift of ∼350 mV in the CO electrooxidation overpotential at the interfacial site of the NiO(111)/Pt_{55} system compared to the unsupported Pt_{55} NP. The enhancement is attributed to the simultaneous weaker binding energy of CO and stronger binding energy of OH when the Pt_{55} NP is in contact with NiO(111) compared to when Pt_{55} NP is unsupported. These results are in qualitative agreement with the CV experiments, where negative shifts in the CO electrooxidation peak potentials were observed on PtNPs supported on $Ni_{0.9}O$ thin films, compared to when support interactions were absent.

Bader Charge Analysis. We performed Bader charge analysis to examine the effect of the electronic states of the active sites of our model structures on CO binding energy. The results are summarized in Figure S15 and Table S7 in the SI. The analysis reveals decreased electron density on Pt_{55} NP supported on NiO(111). This decrease leads to electron-deficient active sites that have a weaker binding energy of CO compared to the isolated Pt_{55} NP. Thus, we suggest that the electronic equilibration, defined as the point at which charge transfer is complete and the optimal electronic state is achieved,[75] between Pt_{55} NP and NiO(111) is responsible for the enhanced CO electrooxidation activity of the NiO(111)/Pt_{55} system.

It is important to note that experimentally, we did not observe changes in the electronic state of the PtNPs regardless of whether they are or are not in contact with the $Ni_{0.9}O$ supports. This discrepancy between theory and experiment arises from the nature of XPS, which measures the average electronic state of the analyzed surface rather than the specific active site that is examined using DFT.

SUMMARY AND CONCLUSIONS

To summarize, we used a well-defined experimental model to investigate SMSIs between PtNPs and $Ni_{0.9}O$ thin films and their effects on CO electrooxidation reaction. We observed significant negative shifts in CO electrooxidation peak potentials and OER suppression when PtNPs were directly supported on $Ni_{0.9}O$ thin films compared to when support interactions were absent. As a part of control experiments, we showed that there is no change in the electrocatalytic activity of PtNPs for the CO electrooxidation reaction regardless of whether they are in contact with the SMSI passive PPF electrode.

The experimentally observed results were validated with DFT, where simultaneous enhancement of CO electrooxidation and suppression of OER activity on $Ni_{0.9}O$-supported PtNPs were attributed to the decrease of the binding energy of CO and an increase of the binding energy of OH at the interfacial site between Pt_{55} NP and NiO(111) compared to the isolated Pt_{55} NP. The change in the binding energies of the reactants is attributed to the electronic equilibration between Pt_{55} NP and NiO(111). Importantly, the results shown in this study indicate that the theoretical/experimental approach used in our previous reports for electrochemical reductions is also applicable to electrooxidation reactions.

ASSOCIATED CONTENT

Supporting Information

The Supporting Information is available free of charge at https://pubs.acs.org/doi/10.1021/acs.jpcc.2c08254.

Pt DENs syntheses; TEM micrographs and particle-size distributions; DFT model structures; thickness analysis of ALD films; stability test data; optical profilometry; high-resolution XPS spectra; CO electrooxidation data; and Gibbs free energy diagrams (PDF)

AUTHOR INFORMATION

Corresponding Authors

Graeme Henkelman − *Department of Chemistry and Oden Institute for Computational Engineering and Science, The University of Texas at Austin, Austin, Texas 78712-1224, United States;* orcid.org/0000-0002-0336-7153; Email: henkelman@utexas.edu

Richard M Crooks − *Department of Chemistry, Center for Electrochemistry, and Texas Materials Institute, The University of Texas at Austin, Austin, Texas 78712-1224, United States;* orcid.org/0000-0001-5186-4878; Email: crooks@cm.utexas.edu

https://doi.org/10.1021/acs.jpcc.2c08254
J Phys Chem C 2023 127 7107−7118

Authors

Aigerim Galyamova − *Department of Chemistry and Center for Electrochemistry, The University of Texas at Austin, Austin, Texas 78712-1224, United States*

Hyunwoo Ha − *Department of Chemistry and Oden Institute for Computational Engineering and Science, The University of Texas at Austin, Austin, Texas 78712-1224, United States*

Complete contact information is available at: https://pubs.acs.org/10.1021/acs.jpcc.2c08254

Author Contributions

⊥A.G. and H.H. contributed equally to this work.

Notes

The authors declare no competing financial interest.

■ ACKNOWLEDGMENTS

The authors gratefully acknowledge support from the Chemical Sciences, Geosciences, and Biosciences Division, Office of Basic Energy Sciences, Office of Science, U.S. Department of Energy (Contract: DE-SC0010576). They also thank the Robert A. Welch Foundation (RMC: Grant F-0032 and GH: Grant F-1841) for sustained support of our research.

■ REFERENCES

(1) Ostojic, N.; Duan, Z.; Galyamova, A.; Henkelman, G.; Crooks, R. M. Electrocatalytic Study of the Oxygen Reduction Reaction at Gold Nanoparticles in the Absence and Presence of Interactions with SnO_x Supports. *J. Am. Chem. Soc.* **2018**, *140*, 13775−13785.

(2) Galyamova, A.; Shin, K.; Henkelman, G.; Crooks, R. M. Effect of TiO_x Substrate Interactions on the Electrocatalytic Oxygen Reduction Reaction at Au Nanoparticles. *J. Phys. Chem. C* **2020**, *124*, 10045−10056.

(3) Vielstich, W.; Lamm, A.; Gasteiger, H. A. *Handbook of Fuel Cells: Fundamentals Technology and Applications*; Wiley: Chichester, U.K., 2003; Vol. 2.

(4) Skulason, E.; Jónsson, H. Atomic Scale Simulations of Heterogeneous Electrocatalysis: Recent Advances. *Adv. Phys.: X* **2017**, *2*, 481−495.

(5) Ostojic, N.; Thorpe, J. H.; Crooks, R. M. Electron Transfer Facilitated by Dendrimer-Encapsulated Pt Nanoparticles Across Ultrathin, Insulating Oxide Films. *J. Am. Chem. Soc.* **2016**, *138*, 6829−6837.

(6) Ostojic, N.; Crooks, R. M. Electrocatalytic Reduction of Oxygen on Platinum Nanoparticles in the Presence and Absence of Interactions with the Electrode Surface. *Langmuir* **2016**, *32*, 9727−9735.

(7) Anderson, M. J.; Ostojic, N.; Crooks, R. M. Microelectrochemical Flow Cell for Studying Electrocatalytic Reactions on Oxide-Coated Electrodes. *Anal. Chem.* **2017**, *89*, 11027−11035.

(8) Galyamova, A.; Crooks, R. M. Effect of Intermediate Semiconducting TiO_x Thin Films on Nanoparticle-Mediated Electron Transfer: Electrooxidation of CO. *Nanomaterials* **2022**, *12*, 855.

(9) Bronstein, L. M.; Shifrina, Z. B. Dendrimers as Encapsulating, Stabilizing, or Directing Agents for Inorganic Nanoparticles. *Chem. Rev.* **2011**, *111*, 5301−5344.

(10) Lhenry, S.; Jalkh, J.; Leroux, Y. R.; Ruiz, J.; Ciganda, R.; Astruc, D.; Hapiot, P. Tunneling Dendrimers. Enhancing Charge Transport Through Insulating Layer Using Redox Molecular Objects. *J. Am. Chem. Soc.* **2014**, *136*, 17950−17953.

(11) Myers, V. S.; Weir, M. G.; Carino, E. V.; Yancey, D. F.; Pande, S.; Crooks, R. M. Dendrimer-Encapsulated Nanoparticles: New Synthetic and Characterization Methods and Catalytic Applications. *Chem. Sci.* **2011**, *2*, No. 1632.

(12) An, K.; Alayoglu, S.; Musselwhite, N.; Plamthottam, S.; Melaet, G.; Lindeman, A. E.; Somorjai, G. A. Enhanced CO Oxidation Rates at the Interface of Mesoporous Oxides and Pt Nanoparticles. *J. Am. Chem. Soc.* **2013**, *135*, 16689−16696.

(13) Doornkamp, C.; Ponec, V. The Universal Character of the Mars and Van Krevelen Mechanism. *J. Mol. Catal. A: Chem.* **2000**, *162*, 19−32.

(14) Comignani, V.; Sieben, J. M.; Brigante, M. E.; Duarte, M. M. Carbon Supported Pt−NiO Nanoparticles for Ethanol Electro-Oxidation in Acid Media. *J. Power Sources* **2015**, *278*, 119−127.

(15) Ranganathan, S.; McCreery, R. L. Electroanalytical Performance of Carbon Films with Near-Atomic Flatness. *Anal. Chem.* **2001**, *73*, 893−900.

(16) Trindell, J. A.; Duan, Z.; Henkelman, G.; Crooks, R. M. Well-Defined Nanoparticle Electrocatalysts for the Refinement of Theory. *Chem. Rev.* **2020**, *120*, 814−850.

(17) Zaera, F. Molecular Approaches to Heterogeneous Catalysis. *Coord. Chem. Rev.* **2021**, *448*, No. 214179.

(18) Henkelman, G.; Arnaldsson, A.; Jónsson, H. A Fast and Robust Algorithm for Bader Decomposition of Charge Density. *Comput. Mater. Sci.* **2006**, *36*, 354−360.

(19) Anderson, R. M.; Yancey, D. F.; Loussaert, J. A.; Crooks, R. M. Multistep Galvanic Exchange Synthesis Yielding Fully Reduced Pt Dendrimer-Encapsulated Nanoparticles. *Langmuir* **2014**, *30*, 15009−15015.

(20) Pande, S.; Weir, M. G.; Zaccheo, B. A.; Crooks, R. M. Synthesis, Characterization, and Electrocatalysis Using Pt and Pd Dendrimer-Encapsulated Nanoparticles Prepared by Galvanic Exchange. *New J. Chem.* **2011**, *35*, 2054−2060.

(21) Kaatz, F. H.; Bultheel, A. Magic Mathematical Relationships for Nanoclusters. *Nanoscale Res. Lett.* **2019**, *14*, No. 150.

(22) Aarons, J.; Sarwar, M.; Thompsett, D.; Skylaris, C.-K. Perspective: Methods for Large-Scale Density Functional Calculations on Metallic Systems. *J. Chem. Phys.* **2016**, *145*, No. 220901.

(23) Ye, H.; Crooks, J. A.; Crooks, R. M. Effect of Particle Size on the Kinetics of the Electrocatalytic Oxygen Reduction Reaction Catalyzed by Pt Dendrimer-Encapsulated Nanoparticles. *Langmuir* **2007**, *23*, 11901−11906.

(24) Powell, C. *X-ray Photoelectron Spectroscopy Database XPS*. version 4.1, NIST Standard Reference Database 20, 1989.

(25) Kresse, G.; Furthmuller, J. Efficiency of Ab-Initio Total Energy Calculations for Metals and Semiconductors Using a Plane-Wave Basis Set. *Comput. Mater. Sci.* **1996**, *6*, 15−50.

(26) Perdew, J. P.; Burke, K.; Ernzerhof, M. Generalized Gradient Approximation Made Simple. *Phys. Rev. Lett.* **1996**, *77*, 3865−3868.

(27) Blöchl, P. E. Projector Augmented-Wave Method. *Phys. Rev. B* **1994**, *50*, 17953−17979.

(28) Dudarev, S. L.; Botton, G. A.; Savrasov, S. Y.; Humphreys, C. J.; Sutton, A. P. Electron-Energy-Loss Spectra and the Structural Stability of Nickel Oxide: An LSDA+U Study. *Phys. Rev. B* **1998**, *57*, 1505−1509.

(29) Wang, L.; Maxisch, T.; Ceder, G. Oxidation Energies of Transition Metal Oxides Within the GGA+*U* Framework. *Phys. Rev. B* **2006**, *73*, No. 195107.

(30) Zhao, W.; Bajdich, M.; Carey, S.; Vojvodic, A.; Nørskov, J. K.; Campbell, C. T. Water Dissociative Adsorption on NiO(111): Energetics and Structure of the Hydroxylated Surface. *ACS Catal.* **2016**, *6*, 7377−7384.

(31) Fiévet, F.; Germi, P.; Bergevin, F. de.; Figlarz, M. Lattice Parameter, Microstrains and Non-stoichiometry in NiO. Comparison Between Mosaic Microcrystals and Quasi-Perfect Single Microcrystals. *J. Appl. Crystallogr.* **1979**, *12*, 387−394.

(32) Yoshihara, J.; Parker, S. C.; Campbell, C. T. Island Growth Kinetics During Vapor Deposition of Cu Onto the Zn-Terminated ZnO(0001) Surface. *Surf. Sci.* **1999**, *439*, 153−162.

(33) Cheetham, A. K.; Hope, D. A. O. Magnetic Ordering and Exchange Effects in the Antiferromagnetic Solid Solutions $Mn_xNi_{1-x}O$. *Phys. Rev. B* **1983**, *27*, 6964−6967.

(34) Davó-Quinonero, A.; Bailón-García, E.; López-Rodríguez, S.; Juan-Juan, J.; Lozano-Castelló, D.; García-Melchor, M.; Herrera, F. C.; Pellegrin, E.; Escudero, C.; Bueno-López, A. Insights into the

Oxygen Vacancy Filling Mechanism in CuO/CeO_2 Catalysts: A Key Step Toward High Selectivity in Preferential CO Oxidation. *ACS Catal.* **2020**, *10*, 6532−6545.
(35) Burgel, C.; Reilly, N. M.; Johnson, G. E.; Mitric, R.; Kimble, M. L.; Castleman, A. W.; Bonacic-Koutecky, V. Influence of Charge State on the Mechanism of CO Oxidation on Gold Clusters. *J. Am. Chem. Sci.* **2008**, *130*, 1694−1698.
(36) Zhang, L.; Kim, H. Y.; Henkelman, G. CO Oxidation at the Au−Cu Interface of Bimetallic Nanoclusters Supported on CeO_2(111). *J. Phys. Chem. Lett.* **2013**, *4*, 2943−2947.
(37) Tiwari, A.; Heenen, H. H.; Bjørnlund, A. S.; Hochfilzer, D.; Chan, K.; Horch, S. Electrochemical Oxidation of CO on Cu Single Crystals Under Alkaline Conditions. *ACS Energy Lett.* **2020**, *5*, 3437−3442.
(38) Duan, Z.; Henkelman, G. Calculations of the pH-Dependent Onset Potential for CO Electrooxidation on Au(111). *Langmuir* **2018**, *34*, 15268−15275.
(39) Nørskov, J. K.; Rossmeisl, J.; Logadottir, A.; Lindqvist, L.; Kitchin, J. R.; Bligaard, T.; Jónsson, H. Origin of the Overpotential for Oxygen Reduction at a Fuel-Cell Cathode. *J. Phys. Chem. B* **2004**, *108*, 17886−17892.
(40) Man, I. C.; Su, H.-Y.; Calle-Vallejo, F.; Hansen, H. A.; Martínez, J. I.; Inoglu, N. G.; Kitchin, J.; Jaramillo, T. F.; Nørskov, J. K.; Rossmeisl, J. Universality in Oxygen Evolution Electrocatalysis on Oxide Surfaces. *ChemCatChem* **2011**, *3*, 1159−1165.
(41) Peterson, A. A.; Abild-Pedersen, F.; Studt, F.; Rossmeisl, J.; Nørskov, J. K. How Copper Catalyzes the Electroreduction of Carbon Dioxide Into Hydrocarbon Fuels. *Energy Environ. Sci.* **2010**, *3*, No. 1311.
(42) Richey, N. E.; de Paula, C.; Bent, S. F. Understanding Chemical and Physical Mechanisms in Atomic Layer Deposition. *J. Chem. Phys.* **2020**, *152*, No. 40902.
(43) Holden, K. E. K.; Dezelah, C. L.; Conley, J. F. Atomic Layer Deposition of Transparent p-Type Semiconducting Nickel Oxide Using $Ni(tBu2DAD)_2$ and Ozone. *ACS Appl. Mater. Interfaces* **2019**, *11*, 30437−30445.
(44) Ismail, R. A.; Ghafori, S.; Kadhim, G. A. Preparation and Characterization of Nanostructured Nickel Oxide Thin Films by Spray Pyrolysis. *Appl. Nanosci.* **2013**, *3*, 509−514.
(45) Kim, D. S.; Lee, H. C. Nickel Vacancy Behavior in the Electrical Conductance of Nonstoichiometric Nickel Oxide Film. *J. Appl. Phys.* **2012**, *112*, No. 34504.
(46) Karsthof, R.; Anton, A. M.; Kremer, F.; Grundmann, M. Nickel Vacancy Acceptor in Nickel Oxide: Doping Beyond Thermodynamic Equilibrium. *Phys. Rev. Mater.* **2020**, *4*, No. 034601.
(47) Ramanathan, S.; Chi, D.; McIntyre, P. C.; Wetteland, C. J.; Tesmer, J. R. Ultraviolet-Ozone Oxidation of Metal Films. *J. Electrochem. Soc.* **2003**, *150*, No. F110.
(48) Yang, T. S.; Cho, W.; Kim, M.; An, K.-S.; Chung, T.-M.; Kim, C. G.; Kim, Y. Atomic Layer Deposition of Nickel Oxide Films Using Ni(dmamp)2 and Water. *J. Vac. Sci. Technol., A* **2005**, *23*, 1238−1243.
(49) Reier, T.; Oezaslan, M.; Strasser, P. Electrocatalytic Oxygen Evolution Reaction (OER) on Ru, Ir, and Pt Catalysts: A Comparative Study of Nanoparticles and Bulk Materials. *ACS Catal.* **2012**, *2*, 1765−1772.
(50) Sheng, W.; Gasteiger, H. A.; Shao-Horn, Y. Hydrogen Oxidation and Evolution Reaction Kinetics on Platinum: Acid vs Alkaline Electrolytes. *J. Electrochem. Soc.* **2010**, *157*, No. B1529.
(51) Anderson, R. M.; Zhang, L.; Wu, D.; Brankovic, S. R.; Henkelman, G.; Crooks, R. M. A Theoretical and Experimental In-Situ Electrochemical Infrared Spectroscopy Study of Adsorbed CO on Pt Dendrimer-Encapsulated Nanoparticles. *J. Electrochem. Soc.* **2016**, *163*, H3061−H3065.
(52) Cherstiouk, O.; Simonov, P.; Zaikovskii, V.; Savinova, E. CO Monolayer Oxidation at Pt Nanoparticles Supported on Glassy Carbon Electrodes. *J. Electroanal. Chem.* **2003**, *554*−*555*, 241−251.
(53) Weir, M. G.; Myers, V. S.; Frenkel, A. I.; Crooks, R. M. In Situ X-ray Absorption Analysis of <1.8 nm Dendrimer-Encapsulated Pt Nanoparticles During Electrochemical CO Oxidation. *ChemPhysChem* **2010**, *11*, 2942−2950.
(54) Arenz, M.; Mayrhofer, K. J. J.; Stamenkovic, V.; Blizanac, B. B.; Tomoyuki, T.; Ross, P. N.; Markovic, N. M. The Effect of the Particle Size on the Kinetics of CO Electrooxidation on High Surface Area Pt Catalysts. *J. Am. Chem. Soc.* **2005**, *127*, 6819−6829.
(55) Takasu, Y.; Ohashi, N.; Zhang, X.-G.; Murakami, Y.; Minagawa, H.; Sato, S.; Yahikozawa, K. Size Effects of Platinum Particles on the Electroreduction of Oxygen. *Electrochim. Acta* **1996**, *41*, 2595−2600.
(56) Bard, A. J.; Faulkner, L. R. *Electrochemical Methods: Fundamentals and Applications*, 2nd ed.; John Wiley: New York, USA, 2001.
(57) Moulder, J. F.; Stickle, W. F.; Sobol, P. E.; Bomben, K. D. *Handbook of X-ray Photoelectron Spectroscopy: A Reference Book of Standard Spectra for Identification and Interpretation of XPS Data*; Perkin-Elmer Corporation: Eden Prairie, Minnesota, USA, 1992.
(58) Mansour, A. N. Characterization of NiO by XPS. *Surf. Sci. Spectra* **1994**, *3*, 231−238.
(59) Liu, P.; Logadottir, A.; Nørskov, J. K. Modeling the Electro-Oxidation of CO and H_2/CO on Pt, Ru, PtRu and Pt_3Sn. *Electrochim. Acta* **2003**, *48*, 3731−3742.
(60) Grabow, L. C.; Hvolbæk, B.; Nørskov, J. K. Understanding Trends in Catalytic Activity: The Effect of Adsorbate−Adsorbate Interactions for CO Oxidation Over Transition Metals. *Top. Catal.* **2010**, *53*, 298−310.
(61) Falsig, H.; Hvolbaek, B.; Kristensen, I. S.; Jiang, T.; Bligaard, T.; Christensen, C. H.; Nørskov, J. K. Trends in the Catalytic CO Oxidation Activity of Nanoparticles. *Angew. Chem., Int. Ed.* **2008**, *47*, 4835−4839.
(62) Abild-Pedersen, F.; Greeley, J.; Studt, F.; Rossmeisl, J.; Munter, T. R.; Moses, P. G.; Skulason, E.; Bligaard, T.; Nørskov, J. K. Scaling Properties of Adsorption Energies for Hydrogen-Containing Molecules on Transition-Metal Surfaces. *Phys. Rev. Lett.* **2007**, *99*, No. 016105.
(63) Baz, A.; Holewinski, A. Understanding the Interplay of Bifunctional and Electronic Effects: Microkinetic Modeling of the CO Electro-Oxidation Reaction. *J. Catal.* **2020**, *384*, 1−13.
(64) Narayanasamy, J.; Anderson, A. B. Mechanism for the Electrooxidation of Carbon Monoxide on Platinum by H_2O. Density Functional Theory Calculation. *J. Electroanal. Chem.* **2003**, *554*−*555*, 35−40.
(65) McPherson, I. J.; Ash, P. A.; Jones, L.; Varambhia, A.; Jacobs, R. M. J.; Vincent, K. A. Electrochemical CO Oxidation at Platinum on Carbon Studied through Analysis of Anomalous in Situ IR Spectra. *J. Phys. Chem. C* **2017**, *121*, 17176−17187.
(66) Calle-Vallejo, F.; Martínez, J. I.; García-Lastra, J. M.; Sautet, P.; Loffreda, D. Fast Prediction of Adsorption Properties for Platinum Nanocatalysts with Generalized Coordination Numbers. *Angew. Chem., Int. Ed.* **2014**, *53*, 8316−8319.
(67) Choi, Y.; Cha, S. K.; Ha, H.; Lee, S.; Seo, H. K.; Lee, J. Y.; Kim, H. Y.; Kim, S. O.; Jung, W. Unravelling Inherent Electrocatalysis of Mixed-Conducting Oxide Activated by Metal Nanoparticle for Fuel Cell Electrodes. *Nat. Nanotechnol.* **2019**, *14*, 245−251.
(68) Yoo, M.; Yu, Y.-S.; Ha, H.; Lee, S.; Choi, J.-S.; Oh, S.; Kang, E.; Choi, H.; An, H.; Lee, K.-S.; et al. A Tailored Oxide Interface Creates Dense Pt Single-Atom Catalysts With High Catalytic Activity. *Energy Environ. Sci.* **2020**, *13*, 1231−1239.
(69) Yoon, S.; Ha, H.; Kim, J.; Nam, E.; Yoo, M.; Jeong, B.; Kim, H. Y.; An, K. Influence of the Pt Size and CeO_2 Morphology at the Pt−CeO_2 Interface in CO Oxidation. *J. Mater. Chem. A* **2021**, *9*, 26381−26390.
(70) Ooka, H.; Huang, J.; Exner, K. S. The Sabatier Principle in Electrocatalysis: Basics, Limitations, and Extensions. *Front. Energy Res.* **2021**, *9*, No. 654460.
(71) Koper, M. T. Thermodynamic Theory of Multi-Electron Transfer Reactions: Implications for Electrocatalysis. *J. Electroanal. Chem.* **2011**, *660*, 254−260.
(72) Laursen, A. B.; Varela, A. S.; Dionigi, F.; Fanchiu, H.; Miller, C.; Trinhammer, O. L.; Rossmeisl, J.; Dahl, S. Electrochemical

https://doi.org/10.1021/acs.jpcc.2c08254
J Phys Chem C 2023 127 7107−7118

Hydrogen Evolution: Sabatier's Principle and the Volcano Plot. *J. Chem. Educ.* **2012**, *89*, 1595−1599.
(73) Sabatier, P. Hydrogenations et Deshydrogenations par Catalyse. *Ber. Dtsch. Chem. Ges.* **1911**, *44*, 1984−2001.
(74) Yu, L.; Liu, Y.; Yang, F.; Evans, J.; Rodriguez, J. A.; Liu, P. CO Oxidation on Gold-Supported Iron Oxides: New Insights into Strong Oxide−Metal Interactions. *J. Phys. Chem. C* **2015**, *119*, 16614−16622.
(75) Pacchioni, G. Electronic Interactions and Charge Transfers of Metal Atoms and Clusters on Oxide Surfaces. *Phys. Chem. Chem. Phys.* **2013**, *15*, 1737−1757.

https://doi.org/10.1021/acs.jpcc.2c08254
J Phys Chem C 2023 127 7107−7118